FLUID–STRUCTURAL INTERACTION WITH APPLICATION TO ROCKET ENGINES

E. LEFRANÇOIS[a,*], G. DHATT[b] AND D. VANDROMME[a]

[a] *LMFN, CORIA, UMR CNRS 6614, Université and Insa de Rouen, Campus du Madrillet,*
Avenue de l'Université BP8, 76801, St. Etienne du Rouvray, France
[b] *LMR, Département de Mécanique, URA CNRS 2213, Université and Insa de Rouen, Campus du Madrillet,*
Avenue de l'Université BP8, 76801, St. Etienne du Rouvray, France

SUMMARY

The objective of this work is to develop a finite element model for studying fluid–structure interaction. The geometrically non-linear structural behaviour is considered and based on large rotations and large displacements. An arbitrary Lagrangian–Eulerian (ALE) formulation is used to represent the compressible inviscid flow with moving boundaries. The structural response is obtained using Newmark-type time integration and fluid response employs the Lax–Wendroff scheme. A number of numerical examples are presented to validate the structural model, moving mesh implantation of the ALE model and complete fluid–structure interaction. Copyright © 1999 John Wiley & Sons, Ltd.

KEY WORDS: geometrical non-linearities; actualized Lagrangian formulation; moving boundaries; ALE formulation; Lax–Wendroff; FCT; finite elements

1. INTRODUCTION

The structural components of rocket engines may undergo large displacements during engine start-up, shut-down or nominal running phases. In general, the influence of structural modifications is neglected in traditional computational fluid dynamics. The structural behaviour is calculated in a decoupled manner with parietal forces obtained from fluid flow calculations. Various components of rocket-type structures may be very flexible and undergo large displacements. The influence of structural modifications on fluid flow may be studied in the following simple manner:

1. at any instant *t* and for a known geometry, we perform the fluid flow calculations with known boundary displacements based on an Eulerian description;
2. the resulting surface forces are used to calculate the structural response using a Lagrangian approach;
3. the geometry and the mesh are updated. Step 1 is repeated and so on . . .

This approach for fluid–structure interaction is very simple since existing models may be coupled through a simple data transfer interface. However, for large structure displacements, the mesh configuration could have strong distortions and mesh updating techniques would become cumbersome and erroneous.

---

* Correspondence to: LMFN, CORIA, UMR CNRS 6614, Université and Insa de Rouen, Campus du Madrillet, Avenue de l'Université BP8, 76801, St. Etienne du Rouvray, France. E-mail: lefranco@coria.fr

In recent years, a significant research effort has been devoted to the development of numerical models for studying fluid–structure interactions in a general way. These models have the following characteristics:

– a Lagrangian or an updated Lagrangian formulation is used to represent the structural behaviour with geometrical non-linearities [1–7].
– an arbitrary Lagrangian–Eulerian (ALE) formulation is employed to represent the fluid flow behaviour. If the boundary of the flow domain is fixed, one usually uses the Eulerian description. The Lagrangian description is derived from the structural displacement that corresponds to a part of the boundary of the domain [8–12]. Space discretization is obtained through finite elements or finite volumes techniques. Using an ALE formulation, one may consider large displacements of mesh nodes keeping minimum element distortions.

In this study, the authors present a finite element ALE formulation for studying compressible flows with large structural movements. In the following section, the mathematical and finite element models employed for such problems are presented. Particular attention is given to the choice of numerical schemes, such as the Lax–Wendroff scheme with a technique of shock capturing based on the flux corrected transport (FCT) for fluid and mesh node velocities. A number of examples are presented to validate and assess the efficiency of the coupled model.

2. MATHEMATICAL MODEL

The fluid–structure interaction model can be divided in three parts:

– a Lagrangian structural model with large rotations and displacements to include beams, plates and shells.
– an ALE formulation for compressible inviscid flows.
– a description for a moving configuration (fluid domain) compatible with kinematic conditions relative to moving boundaries.

In this section, mathematical relations describing the structural and fluid behaviours will be discussed.

2.1. Structural analysis model

The mathematical model is based on the Lagrangian or material description in order to describe the structural behaviour with geometrical non-linearities. Different aspects of the model may be presented as follows:
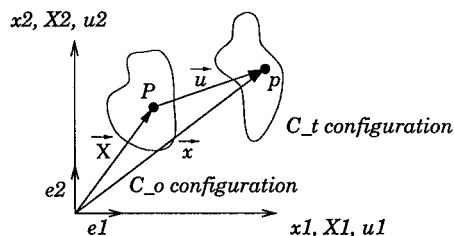

Figure 1. Position vector.

2.1.1. Kinematic relations. The position vector in a deformed position using a Lagrangian description is (Figure 1):

$$\vec{x} = \vec{X} + \vec{u}(x, t),$$

where $\vec{X}$ is the position vector in the C_0 configuration occupied by the solid at instant '0'; $\vec{x}$ the position vector in the current configuration C_t, which is a function of $\vec{X}$ and t; and $\vec{u}$ the displacement vector function of $\vec{X}$ and t.

The tensor of deformation gradients **F** defines the local transformation between two configurations:

$$\mathrm{d}\vec{x} = [F]\,\mathrm{d}\vec{X}, \quad \text{where } [F] = \left[[I] + \frac{\partial \vec{u}}{\partial \vec{X}} \right]. \tag{1}$$

The Green–Lagrange deformation tensor is defined by

$$(\mathrm{d}\vec{x} \cdot \mathrm{d}\vec{x} - \mathrm{d}\vec{X} \cdot \mathrm{d}\vec{X}) = 2\,\mathrm{d}\vec{X} \cdot \varepsilon \cdot \mathrm{d}\vec{X} = 2\langle \mathrm{d}X \rangle [\varepsilon]\{\mathrm{d}X\},$$

with

$$[\varepsilon] = \frac{1}{2}[F^T \cdot F - I]. \tag{2}$$

Remark:

In this presentation, the authors systematically employ a single Cartesian system for structural and fluid quantities. Thus, all vectors and tensors are written in component form as column or line vectors and matrices.

The way to pass from an integral over C_t to C_0 is

$$\int_{V_t} (\dots)\,\mathrm{d}V = \int_{v_0} (\dots)\det(F)\,\mathrm{d}V_0,$$

and for integrals over surfaces, we have

$$\vec{n}\,\mathrm{d}S = \mathbf{F}^{-T}\vec{n}_0\,\mathrm{d}S_0,$$

where $\vec{n}$ and $\vec{n}_0$ are unit normal vectors associated to $\mathrm{d}S$ and $\mathrm{d}S_0$ respectively. The polar decomposition of tensor **F** gives

$$[F] = [R][U],$$

with $[R]$ the pure rotation matrix between two configurations; and $[U]$ the pure deformation matrix, define positive.

2.1.2. Stress tensor and equilibrium relations. The Cauchy stress tensor σ in C_t configuration is related to the Piola–Kirchhoff tensor **S** transported to C_0 configuration using the same Cartesian co-ordinate system:

$$[\sigma] = [F][S][F]^T \cdot \det(F).$$

Indeed, the tensor **S** corresponds to the contravariant components of σ in the covariant base defined by **F**.

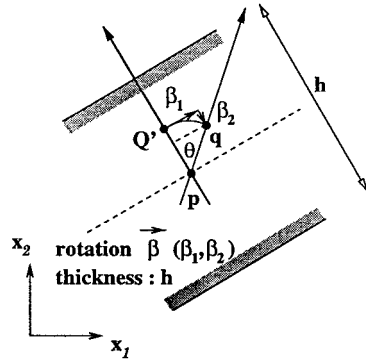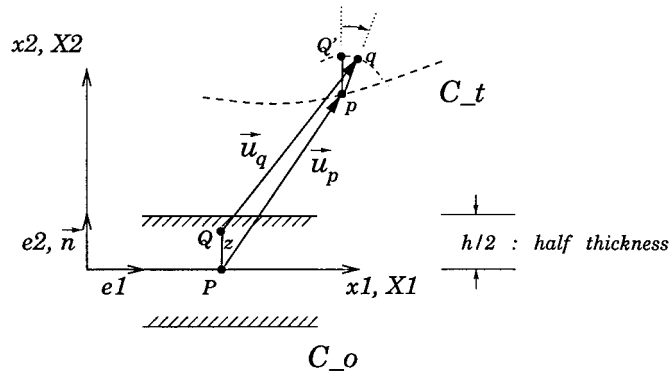The equilibrium relations are written in a weak form often called virtual work or variational form,

Figure 2. Beam formulation.

$$W = \int_{V_t} \vec{\delta u} \rho \frac{\mathrm{d}^2 \vec{u}}{\mathrm{d}t^2} \, \mathrm{d}V + \int_{V_t} \delta D : \sigma \, \mathrm{d}V - \int_{V_t} \vec{\delta u} \vec{f_v} \, \mathrm{d}V - \int_{S_t} \vec{\delta u} \vec{f_s} \, \mathrm{d}S = 0.$$

In the reference configuration C_0, it gives (using the Piola identity):

$$W = \int_{V_0} \vec{\delta u} \rho_0 \frac{\mathrm{d}^2 \vec{u}}{\mathrm{d}t^2} \, \mathrm{d}V_0 + \int_{V_0} \delta \varepsilon : S \, \mathrm{d}V_0 - \int_{V_0} \vec{\delta u} \vec{f_{v0}} \, \mathrm{d}V_0 - \int_{S_0} \vec{\delta u} \vec{f_{s0}} \, \mathrm{d}S_0 = 0, \tag{3}$$

where $\rho_0 = \rho \cdot J$ is the mass conservation; $\delta \vec{u}$ the virtual displacement or test functions using a Galerkin-type formulation; $\delta \varepsilon = \frac{1}{2} \delta [F^T \cdot F - I] = \frac{1}{2} [\delta F^T \cdot F + F^T \delta F]$; δ the variation; $\vec{f_{s0}}, \vec{f_{v0}}$ the external forces in reference configuration C_0.

For linear elastic behaviour, with the Green–Lagrange tensor ε assumed small:

$$\mathbf{S} = \mathbf{H} \cdot \varepsilon$$

where H corresponds to the elasticity matrix.

2.1.3. Beam formulation. A local co-ordinate system is chosen such that the X_1 axis in C_0 configuration is along the middle surface and the thickness direction is associated with X_2 using z for the Q position from P (Figure 2).

The position vector in C_t based on the beam approximation, 'plane sections remain plane without elongation', also called the Reissner–Mindlin theory, is:

$$\vec{x}_q = \vec{X}_Q + \vec{u}_p + z \cdot \vec{\beta}, \quad \text{with} \quad -\frac{h}{2} \leq z \leq \frac{h}{2}.$$

In component form we have: $(X_2 \equiv z)$

$$\begin{Bmatrix} x_1 \\ x_2 \end{Bmatrix}_q = \begin{Bmatrix} X_1 \\ z \end{Bmatrix} + \begin{Bmatrix} u_1(X_1, t) \\ u_2(X_1, t) \end{Bmatrix} + z \begin{Bmatrix} \beta_1(X_1, t) \\ \beta_2(X_2, t) \end{Bmatrix}.$$

The deformation gradient **F** is given by (1):

$$[F] = [\vec{a} + z\vec{b}_{,X_1} \quad \vec{b}],$$

where

$$\vec{a} = \begin{Bmatrix} 1 + u_{1,X_1} \\ u_{2,X_1} \end{Bmatrix}, \qquad \vec{b} = \begin{Bmatrix} \beta_1 \\ 1 + \beta_2 \end{Bmatrix}, \quad \text{with} \quad \vec{b} \cdot \vec{b} = 1.$$

By keeping only the linear terms in z, the deformation tensor (2) becomes

$$[\varepsilon] = \begin{bmatrix} \frac{1}{2}(\vec{a} \cdot \vec{a} - 1) + z\vec{a} \cdot \vec{b}_{,X_1} & \frac{1}{2}\vec{a} \cdot \vec{b} \\ \frac{1}{2}\vec{a} \cdot \vec{b} & 0 \end{bmatrix} = \begin{bmatrix} \varepsilon_m + z\chi & \frac{1}{2}\gamma \\ \frac{1}{2}\gamma & 0 \end{bmatrix}.$$

Remark:

By assuming that deformations are small ($\det(F) = 1$, $[F] \approx [R]$), the components of **S** in the (X_1, X_2) system correspond to the components of σ expressed in the rotated system **R**.

Thus, we have

$$[\sigma] = [R][S][R]^T.$$

The internal virtual work may be written as

$$W_{\text{int}} = \int_{V_0} \delta\varepsilon : S \, dV_0, \quad dV_0 = dA \cdot dX_1,$$

with

$$[S] = \begin{bmatrix} E(\varepsilon_m + z\chi) & \frac{1}{2}G\gamma \\ \frac{1}{2}G\gamma & 0 \end{bmatrix}.$$

If material properties are symmetrical along the thickness direction, we finally obtain

$$W_{\text{int}} = \int_0^L (\delta\varepsilon_m \cdot N + \delta\chi \cdot M + \delta\gamma \cdot T) \, dX_1,$$

where the internal efforts are given by

$$N = \int_A E\varepsilon_m \, dA = H_m \varepsilon_m, \qquad M = \int_A Ez^2\chi \, dA = H_f \chi, \qquad T = \int_A G\gamma \, dA = H_c \gamma.$$

The incremental form associated with the internal virtual work is

$$\Delta W_{\text{int}} = \int_0^L \left(\underbrace{(\delta\Delta\varepsilon_m N + \delta\Delta\chi M + \delta\Delta\gamma T)}_{\text{geom. non-linearities}} + \underbrace{(\delta\varepsilon_m \Delta N + \delta\chi \Delta M + \delta\gamma \Delta T)}_{\text{linear}} \right) dX_1. \tag{4}$$

2.2. ALE fluid model

In general, the mathematical relations of fluid flow are written in an Eulerian framework. The authors present a conservation law in a general description, which may be Eulerian, Lagrangian or some arbitrary description called ALE. A common Cartesian co-ordinate system is employed for these descriptions.

2.2.1. Conservation law for a scalar quantity. For a better understanding, presented first is the conservation law for a scalar quantity $\hat{C}$ in a fluid flow with convection and diffusion. The general form of the conservation law for a control volume $\hat{V}(t)$ is

RATE OF ACCUMULATION + SURFACE EXCHANGE + PRODUCTION = 0.

At any instant t, the flow velocity and the control volume velocity of surface point $\hat{p}$ are respectively, $\hat{v}$ and $\hat{w}$. The description of all quantities is in terms of position vector $\vec{\hat{x}}$ relative to $\hat{V}(t)$ (Figure 3).

The conservation law is written as

$$\frac{\partial}{\partial t}\int_{\hat{V}}\hat{C}(\hat{x},t)\,\mathrm{d}V+\oint_{\hat{S}}\hat{C}(\vec{\hat{u}}-\vec{\hat{w}})\cdot\vec{n}\,\mathrm{d}S+\oint_{\hat{S}}\vec{\hat{q}}_n\cdot\vec{n}\,\mathrm{d}S+\int_{\hat{V}}\hat{f}_v\,\mathrm{d}V=0,$$

where $\vec{\hat{u}}-\vec{\hat{w}}$ is the relative velocity of fluid related to convective flux; $\vec{\hat{q}}_n$ the diffusive flux; $\hat{f}_v$ the production term.

By using the divergence theorem, we obtain

$$\frac{\partial}{\partial t}\int_{\hat{V}}\hat{C}(\hat{x},t)\,\mathrm{d}V+\int_{\hat{V}}\mathrm{Div}_{\hat{x}}[\hat{C}(\vec{\hat{u}}-\vec{\hat{w}})+\vec{\hat{q}}_n]\,\mathrm{d}V+\int_{\hat{V}}\hat{f}_v\,\mathrm{d}V=0.$$

By performing an integration over a fixed reference volume V_r such that

$$\mathrm{d}V=J(t)\,\mathrm{d}V_r,$$

where J is the Jacobian of the transformation:

$$\vec{\hat{x}}=\vec{\hat{x}}(\vec{\hat{x}}_r,t),\qquad \mathrm{d}\vec{\hat{x}}=\mathbf{F}(t)\,\mathrm{d}\vec{\hat{x}}_r\quad\text{with}\quad\mathbf{F}=\frac{\partial\vec{\hat{x}}}{\partial\vec{\hat{x}}_r}\quad\text{and}\quad J=\det(F),$$

yielding

$$\int_{V_r}\left[\frac{\partial}{\partial t}(J\hat{C})\big|_{\hat{x}}+J\,\mathrm{Div}_{\hat{x}}[[\hat{C}(\vec{\hat{u}}-\vec{\hat{w}})+\vec{\hat{q}}_n]+J\hat{f}_v]\,\mathrm{d}V_r=0,$$
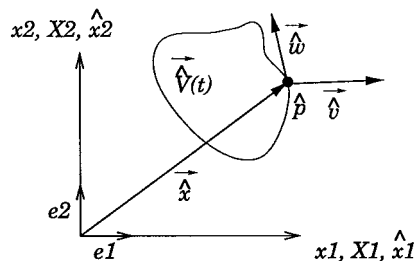
leading to

Figure 3. An arbitrary configuration $\hat{V}(t)$.

$$\frac{\partial}{\partial t}(J\hat{C})\big|_{\hat{x}} + J\,\mathrm{Div}_{\hat{x}}[\hat{C}(\vec{\hat{u}} - \vec{\hat{w}}) + \vec{\hat{q}}_n] + J\hat{f}_v = 0.$$

Remark:

1. In an Eulerian description, the control volume is fixed in time, thus

   $$\hat{w} = 0, \qquad \vec{\hat{x}} = \vec{x}, \qquad \hat{C} = C;$$

   one then obtains

   $$\frac{\partial C}{\partial t} + \mathrm{Div}(C\vec{u} + \vec{q}) + f_v = 0.$$

2. In a Lagrangian description, the control volume moves with the fluid velocity:

   $$\hat{x} = x = X_0 + \phi(X_0, t), \qquad w = u, \qquad \hat{q}_n\,\mathrm{d}\hat{S} = q_{n0}\,\mathrm{d}S_0,$$

   which leads to

   $$\frac{\mathrm{d}C(X_0, t)}{\mathrm{d}t} + \mathrm{Div}\,\vec{q}(X_0, t) + f_v(X_0, t) = 0.$$

   The reference configuration is the fixed Lagrangian position X_0.

3. In a moving finite element mesh, $\vec{\hat{u}}$ is the true fluid velocity at a given position on a mesh point; the reference configuration may simply correspond to the reference element. The control volume velocity $\hat{w}$ is derived from the node mesh velocities.

4. In a previous equation relative to V_r, the time derivative corresponding to $\hat{x}_\mathrm{r}$ is held constant.

5. One can note that the ALE formulation has an effect only on the convective fluxes. Diffusive and turbulent terms are kept unchanged if one accounts for their contribution in the original equation.

   2.2.2. Conservation law for a vectorial quantity in the ALE description. For simplicity, the ALE position $(\hat{x}_1, \hat{x}_2)$ is represented by (x_1, x_2). All quantities projected along the (x_1, x_2) axis will be denoted with the indices 1 and 2 respectively. Source and diffusive terms are set to zero.

   The conservation laws for various quantities of compressible and inviscid flow for a 2D case may thus be written as

$$\frac{\partial}{\partial t}\{JU\}\bigg|_{x_\mathrm{r}} + J\left(\frac{\partial\{F_1\}}{\partial x_1} + \frac{\partial\{F_2\}}{\partial x_2}\right) = 0, \tag{5}$$

where $\{U\}$ denotes the conservative variables; $\{F_1\} = \{F_{c1}\} - w_1\{U\}$ the convective flux along the x_1-direction; $\{F_2\} = \{F_{c2}\} - w_2\{U\}$ the convective flux along the x_2-direction, with

$$\{U\} = \begin{Bmatrix} \rho \\ \rho u_1 \\ \rho u_2 \\ \rho e \end{Bmatrix}, \qquad \{F_{c1}\} = \begin{Bmatrix} \rho u_1 \\ \rho u_1^2 + p \\ \rho u_1 u_2 \\ (\rho e + p)u_1 \end{Bmatrix}, \qquad \{F_{c2}\} = \begin{Bmatrix} \rho u_2 \\ \rho u_1 u_2 \\ \rho u_2^2 + p \\ (\rho e + p)u_2 \end{Bmatrix},$$

with ρ the mass density, u_1 and u_2 the components of fluid velocity in the (x_1, x_2) system respectively, e the total energy per unit of mass and p the local pressure given by the law of a perfect gas

$$p = \rho \cdot r \cdot T = (\gamma - 1)(\rho e - 1/2\rho (u_1^2 + u_2^2)),$$

with the temperature T, $\gamma = 1.4$ and $r = 287$ SI units.

The associated weak form may be written as

$$
\begin{aligned}
W_I &= \int_{V_r} \langle \delta U \rangle \frac{\partial J\{U\}}{\partial t}\, dV_r + \int_{V_r} \langle \delta U \rangle J\left(\frac{\partial \{F_1\}}{\partial x_1} + \frac{\partial \{F_2\}}{\partial x_2}\right) dV_r = 0 \\
&= \frac{\partial}{\partial t} \int_{V(t)} \langle \delta U \rangle \{U\}\, dV + \int_{V(t)} \langle \delta U \rangle \left(\frac{\partial \{F_1\}}{\partial x_1} + \frac{\partial \{F_2\}}{\partial x_2}\right) dV = 0,
\end{aligned}
\tag{6}
$$

where $\langle \delta U \rangle$ is a test function on the reference space.

One obtains another weak form by integrating by parts the second expression:

$$
\begin{aligned}
W_{II} &= \frac{\partial}{\partial t} \int_{V(t)} \langle \delta U \rangle \{U\}\, dV - \int_{V(t)} (\langle \delta U_{,x_1} \rangle \{F_1\} + \langle \delta U_{,x_2} \rangle \{F_2\})\, dV \\
&\quad + \int_{S(t)} \langle \delta U \rangle (\{F_1\} n_x + \{F_2\} n_y)\, dS = 0,
\end{aligned}
\tag{7}
$$

where (n_x, n_y) are the components of the external normal vector at the boundary.

2.3. Displacement description of ALE configuration

The movement of the configuration is defined in the context of finite element description. The reference configuration is naturally taken as the reference element and a proper choice of temporal variation has to be made. The displacement in terms of reference element (ξ, η) is

$$\vec{x}(\vec{\xi}, t) = N_i(\vec{\xi}) \cdot \vec{x}_i(t), \qquad \vec{\xi} = (\xi, \eta).$$

The expression of J is given by

$$
[J(t)] = \det\left[\frac{\partial \vec{x}}{\partial \vec{\xi}}\right] = \det \begin{bmatrix} \dfrac{\partial x_1}{\partial \xi} & \dfrac{\partial x_2}{\partial \xi} \\ \dfrac{\partial x_1}{\partial \eta} & \dfrac{\partial x_2}{\partial \eta} \end{bmatrix}.
\tag{8}
$$

The temporal variation is in general arbitrary but it should satisfy the geometrical and kinematic compatibilities at the boundary with moving structure and should not introduce any mesh distortions. These points are discussed in a following section.

3. FINITE ELEMENT MODEL

This section is devoted to the presentation of finite element models related to structural behaviour, fluid behaviour and mesh movement. The temporal discretization shall also be discussed.

3.1. Beam element with large displacements and rotations

A 2-node element with linear approximation for each variable is used to discretize the geometry (Figure 4)
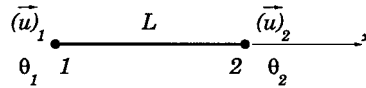
Figure 4. Beam element.

Unknowns are discretized as follows:

$$\hat{u} = \sum_{i=1}^{2} N_i \cdot (\hat{u})_i, \qquad \vec{\beta} = \sum_{i=1}^{2} N_i \begin{Bmatrix} \sin \theta_i \\ \cos \theta_i - 1 \end{Bmatrix},$$

with

$$N_1 = 1 - \frac{x}{L}, \qquad N_2 = \frac{x}{L} \quad \text{and} \quad (\hat{u})_i = \begin{pmatrix} u_1 \\ u_2 \end{pmatrix}_i.$$

The expressions for W and ΔW are discretized using this approximation with a 1-point numerical integration. Each expression is first approximated on each element. It leads to:

$$W = \sum W_{\text{int}}^e + \sum W_m^e + \sum W_{\text{ext}}^e.$$

We have for each term previously introduced in the mathematical structure model:

$$\delta \vec{a} = [B_{ml}]\{\delta u\}, \qquad \delta \vec{b} = [B_f]\{\delta u\}, \qquad \delta \vec{b}_{,x} = [B_c]\{\delta u\}, \tag{9}$$

$$\begin{aligned} W_{\text{int}} &= \int_0^L (\delta \varepsilon_m \cdot N + \delta \chi \cdot M + \delta \gamma \cdot T) \, \mathrm{d}x \\ &= \langle \delta u \rangle L([B_{ml}]^T\{a\}N + ([B_{ml}]^T\{b\}_{,x} + [B_c]^T\{a\})M + ([B_{ml}]^T\{b\} + [B_f]^T\{a\})T) \\ &= \langle \delta u \rangle \underbrace{\{f_{\text{int}}^e\}}_{6 \times 1}. \end{aligned}$$

Concerning the incremental form of the virtual work expression, the discretization leads to

$$\begin{aligned} \Delta W_{\text{int}} &= \int_0^L \left(\underbrace{(\delta \Delta \varepsilon_m N + \delta \Delta \chi M + \delta \Delta \gamma T)}_{\text{geom. non-linearities}} + \underbrace{(\delta \varepsilon_m \Delta N + \delta \chi \Delta M + \delta \gamma \Delta T)}_{\text{linear}} \right) \mathrm{d}x \\ &= \langle \delta u \rangle ([K_\sigma] + [K_{\text{L.Rot.}}] + [K_{\text{Lin.}}])\{\Delta u\} = \langle \delta u \rangle \underbrace{[K_T^e]}_{6 \times 6} \underbrace{\{\Delta u\}}_{6 \times 1}, \end{aligned}$$

where we define $\langle \delta u \rangle = (\langle \delta u_1 \, \delta u_2 \, \delta \theta \rangle_1 \quad \langle \delta u_1 \, \delta u_2 \, \delta \theta \rangle_2)$ are the nodal components of the test function; $\langle \Delta u \rangle = (\langle \Delta u_1 \, \Delta u_2 \, \Delta \theta \rangle_1 \quad \langle \Delta u_1 \, \Delta u_2 \, \Delta \theta \rangle_2)$ the nodal components of the solution increment; $[K_T^e] = [K_\sigma] + [K_{\text{L.Rot.}}] + [K_{\text{Lin.}}]$ the elementary tangent matrix.

After assembling all over the elements, the discretized expression is

$$[M] \left\{ \frac{\partial^2 u}{\partial t^2} \right\} + \{f_{\text{int}}(u, t)\} - \{f_{\text{ext}}\} = 0,$$

where $[M]$ is the global mass matrix; $\{f_{\text{int}}(u, t)\}$ the non-linear internal forces (equivalent to $[K(u, t)]\{u\}$); $\{F_{\text{ext}}\}$ the external forces representing interaction with fluid corresponding to the boundary surface forces.

The Newmark implicit time discretization gives

$$\ddot{u}^{p+1} = \frac{4}{\Delta t^2} (u^{p+1} - u^p) - \frac{4}{\Delta t} \dot{u}^p - \ddot{u}^p,$$

where p and $p+1$ are relative to two successive time steps and Δt is the step size. $\dot{u}$ and $\ddot{u}$ denote the first and second temporal derivatives for u.

Using the above temporal discretization scheme and a Newton–Raphson linearization technique, one obtains

$$-\left[\frac{4}{\Delta t^2}\cdot M + K_T\right]\{\Delta u\} = \{R\},$$

with

$$\{\Delta u\} = \{u^i - u^{i-1}\}^{p+1},$$

$$\{R\} = [M]\left\{\frac{4}{\Delta t}\dot{u}^p + \ddot{u}^p\right\} - \{f_{\text{int}}(u, t)\} + \{F_{\text{ext}}\},$$

the 'i' indice corresponds to iteration number.

Given now is a simple example of validation for a case of large rotations and displacements. The relation between moment M applied to a cantilever beam and its curvature radius Ra is

$$\frac{M}{EI} = \frac{\mathrm{d}^2 U_2}{\mathrm{d}x_1^2} = Ra,$$

with the Young's modulus E and the inertial momentum I.

Numerical results obtained with 40 elements correspond exactly with theoretical values. Different beam configurations after applying $0.9M$ in nine steps are given in Figure 5.

- $E = 21\text{E}10 \text{ N m}^{-2}$, $I = 8.33\text{E} - 8 \text{ m}^4$
- $L = 1 \text{ m}$
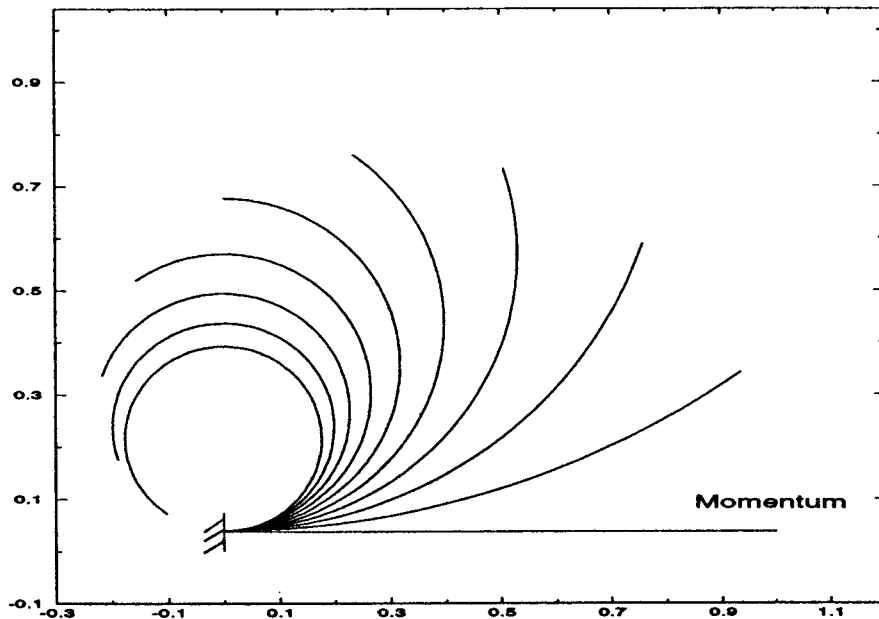- $M = -2744.5 \text{ Nm}$, corresponding to one rolling
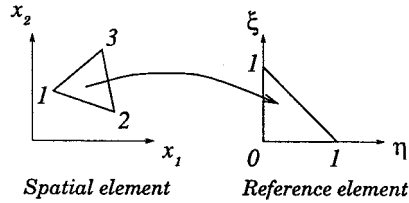

Figure 5. Validation of beam element.

Figure 6. Spatial and reference elements for fluid discretization.

The element has been tested up to three successive rollings for $3M$.

3.2. Fluid finite element model

For a compressible flow, the choice of a finite element model is influenced by the following considerations:

– spatial–temporal discretization should assure stability and ability for shock capturing;
– the temporal scheme should assure uniform field representation for any moving mesh field;
– a proper choice of mesh velocity is necessary, which would be compatible with boundary displacements.

In the present model a central Lax–Wendroff scheme is used, which is conditionally stable but does not assure scheme positivity in high gradient zones. In shocks, it is thus necessary to introduce a shock capturing technique in order to correct the Lax–Wendroff oscillations due to non-positivity. This will be developed in the next section.

The weak form associated with the fluid model and employing temporal discretization is

$$W = \int_{V_r} \langle \delta U \rangle (\{UJ\}^{p+1} - \{UJ\}^p) \, dV_r + \oint_{S_r} [\langle \delta U \rangle (\{F_1\}n_1 + \{F_2\}n_2)]^{p+1/2} J_s^{p+1/2} \, dS_r$$
$$- \int_{V_r} (\langle \delta U \rangle_{,x1} \{F_1\} + \langle \delta U \rangle_{,x2} \{F_2\})^{p+1/2} J_s^{p+1/2} \, dV_r,$$

where $\{F_1\}$ and $\{F_2\}$ are functions of $\{U\}^{p+1/2}$ and calculated on each integration point. Expressions of $\{U\}^{p+1/2}$ will be detailed in the next section.

The expression of the weak form is then split on each element as follows:

$$W = \sum_e W^e.$$

A 3-node triangular element (linear approximation) is employed for space discretization (Figure 6) with the following approximation:

$$x_1(\tau) = \sum_{i=1}^{3} N_i(\xi, \eta) \cdot (x_1(\tau))_i, \qquad x_2(\tau) = \sum_{i=1}^{3} N_i(\xi, \eta) \cdot (x_2(\tau))_i,$$

$$\{U(\tau)\} = \sum_{i=1}^{3} N_i(\xi, \eta) \cdot \{U(\tau)\}_i,$$

$$\{F_1(\tau)\} = \sum_{i=1}^{3} N_i(\xi, \eta) \cdot \{F_1(\tau)\}_i, \qquad \{F_2(\tau)\} = \sum_{i=1}^{3} N_i(\xi, \eta) \cdot \{F_2(\tau)\}_i,$$

and the linear interpolation functions:

Copyright © 1999 John Wiley & Sons, Ltd.

Int. J. Numer. Meth. Fluids **30**: 865–895 (1999)

$$N_1(\xi, \eta) = 1 - \xi - \eta, \qquad N_2(\xi, \eta) = \xi, \qquad N_3(\xi, \eta) = \eta.$$

In an ALE model, the time discretization scheme must be consistent with the variation of nodal co-ordinates $(\check{x}(\tau))_i$. The discretized weak form becomes

$$[M]^{p+1}\{U\}^{p+1} - [M]^p\{U\}^p = \{R\}^{p+1/2},$$

which can be written in an incremental way as

$$[M]^{p+1}\{\Delta U\} = \{R\}^{p+1/2} + ([M]^p - [M]^{p+1})\{U\}^p = \{\mathcal{R}\}, \tag{10}$$

where $[M]^{p+1}$ is the global mass matrix at instant $t + \Delta t$; $[M]^p$ the global mass matrix at instant t; $\{\Delta U\} = \{U\}^{p+1} - \{U\}^p$ the incremental solution; $\{R\}^{p+1/2}$ the global residual vector obtained from $\{U\}^{p+1/2}$ using $F^{p+1/2} = F(\{U\}^{p+1/2})$; $\{\mathcal{R}\}$ the modified residual vector due to $[M]^p$ and $[M]^{p+1}$.

These expressions are calculated exactly using 1-point space integration. To solve (10), two or three Jacobi iterations are performed using diagonalized preconditioned mass matrix (good condition number). Thus, the solution process becomes very efficient.

3.3. Shock capturing technique

In high gradient zones, the non-positive nature of the Lax–Wendroff scheme may produce unwanted oscillations. The idea behind stabilization techniques (flux corrected transport in this case) is to consider a first-order scheme in a high gradient zone and to conserve the higher-order Lax–Wendroff scheme elsewhere.

After resolution of (10) the new solution obtained is

$$\{U\}^{p+1} = \{U\}^p + \{\Delta U\}.$$

The aim is to obtain a $\{\Delta U\}$ of an order as high as possible without introducing overshoots. To this end, the previous equation is rewritten as

$$\{U\}^{p+1} = \{U\}^l + (\{\Delta U\}^h - \{\Delta U\}^l),$$

where $\{\Delta U\}^h$ and $\{\Delta U\}^l$ denote the increments obtained respectively with high- and low-order schemes and $\{U\}^l$ is the monotonic solution of the low-order scheme. The idea behind FCT is to limit the second term on the right-hand-side of the previous equation,

$$\{U\}^{p+1} = \{U\}^l + \lim(\{\Delta U\}^h - \{\Delta U\}^l),$$

in such a way that no new over/undershoots are created.

The high-order solution is obtained after resolution of (10). The low-order solution is obtained after modification of (10) in introducing the lumped mass matrix and adding a damping term as follows:

$$[M_d]\{\Delta U^l\} = \{\mathcal{R}\} + \underbrace{C_d([M] - [M_d])\{U^p\}}_{\text{damping term}}, \quad 0 \le C_d \le 1,$$

with $[M_d]$ the lumped mass matrix (diagonal) and C_d the damping coefficient, usually taken at 0.3.

The identification of high gradient zones is obtained from variables such as pressure or density. These zones are then related to a local limiter $0 < \lim < 1$, which can be computed in different ways. One can cite the estimation of local error (second spatial derivatives) [13] or the elimination of any local extremum in considering elementary contributions of each cell surrounding a node [14,15].

The approach used here for the limiting procedure is directly based on the Löhner approach described in detail in Reference [14].

3.4. Mesh displacement

3.4.1. Geometrical consistency. Suppose that mesh displacement within the interval $(t, t + \Delta t)$ is defined as follows:

$$\vec{x}(\tau) = (1 - \phi(\tau))\vec{x}^p(\xi, \eta) + \phi(\tau)\vec{x}^{p+1}(\xi, \eta),$$

leading to

$$\vec{w}(\xi, \eta) = \dot{\phi}(\vec{x}^{p+1} - \vec{x}^p),$$

with $\phi(\tau = t) = 0$ and $\phi(\tau = t + \Delta t) = 1$.

The Jacobian matrix is obtained in a general way

$$[J]^T = [F(\tau)] = \left[\frac{\partial \vec{x}}{\partial \xi} \frac{\partial \vec{x}}{\partial \eta} \right] = ((1 - \phi(\tau))[F]^p + \phi(\tau)[F]^{p+1}$$

and the determinant is quadratic in ϕ:

$$J(\tau) = \det(F(\tau)) = a_0 + a_1\phi(\tau) + a_2\phi^2(\tau). \tag{11}$$

For a fixed mesh, the Lax–Wendroff finite element model satisfies the consistency and stability conditions (see [13]). For a moving mesh, it is essential that the uniform flow field be exactly conserved (called geometrical consistency law) for any moving mesh. If a uniform flow that corresponds to $\{U\}$ constant is considered, Equation (5) becomes for each component of $\{U\}$:

$$\frac{\partial J}{\partial t} - J \cdot \text{Div } \vec{w} = 0. \tag{12}$$

In weak form, we have

$$\frac{\partial}{\partial t} \int_V \psi \, dV = \int_V \psi \, \text{Div } \vec{w} \, dV,$$

where ψ is a test function representing each component of $\{\delta U\}$. For geometrical consistency it is then essential this relation be exactly satisfied by the discrete model (10). The time integration leads to

$$\int_{V^{p+1}} \psi \, dV - \int_{V^p} \psi \, dV = \int_t^{t+\Delta t} \int_{V_r} \psi \, \text{Div } \vec{w} \, dV_r \, d\tau$$

$$= \int_t^{t+\Delta t} \int_{V_r} \psi \frac{\partial J}{\partial \tau} \, dV_r \, d\tau \quad \text{using (12)}$$

$$= \int_t^{t+\Delta t} \int_{V_r} \psi(a_1\dot{\phi}(\tau) + 2a_2\phi(\tau)\dot{\phi}(\tau)) \, dV_r \, d\tau \quad \text{using (11)}$$

$$= \int_0^1 \int_{V_r} \psi(a_1 + a_2\phi(\tau)) \, dV_r \, d\phi. \tag{13}$$

For a 2D case, the right term in the last equation is linear in $\phi(\tau)$. The space integration is guaranteed by standard finite element integration. Since the variation is linear in $\phi(\tau)$, the midpoint rule integration is sufficient to integrate exactly this last term. In this case, $\phi(\tau)$ has been chosen linear in τ and then the integration point corresponds to $\phi(\tau = \frac{1}{2}) = \frac{1}{2}$. Recalling that we are interested in integrating Div $\vec{w}$, this leads to

$$\int_{V^{p+1}} \psi \, dV - \int_{V^p} \psi \, dV = \Delta t \int_{V^{p+1/2}} \psi \, \text{Div} \, \vec{w} \, dV,$$

which corresponds to an integration over the domain located at $p + 1/2$ and defined by

$$\vec{x}^{p+1/2} = \frac{\vec{x}^{p+1} + \vec{x}^p}{2}.$$

The corresponding mesh field velocity is calculated as follows:

$$\vec{w}^{p+1/2} = \frac{\vec{x}^{p+1} - \vec{x}^p}{\Delta t}.$$

As mentioned in a previous section, the same consideration must be applied to the calculation of $\{U\}^{n+1/2}$ when it is assumed that mesh velocity appears in its expression. Two choices at least may be proposed: the first one is to consider mesh velocity equal to zero and leads to

$$\{U\}^{p+1/2} = \{U\}^p - \frac{\Delta t}{2}\left(\frac{\partial \{F_{c1}\}}{\partial x_1} + \frac{\partial \{F_{c2}\}}{\partial x_2}\right)^p.$$

The second choice (considered here) uses middle point integration between p and $p + 1/2$ and leads to

$$\{JU\}^{p+1/2} = \{JU\}^p - \frac{\Delta t}{2}\left(J\left(\frac{\partial \{F_{c1}\}}{\partial x_1} + \frac{\partial \{F_{c2}\}}{\partial x_2}\right)\right)^{p+1/4}.$$

These two choices satisfy consistency.

3.4.2. Solid boundaries. In order to assure compatibility between fluid and moving boundaries there is a need to respect boundary conditions. For inviscid flows, slip condition is applied near boundaries (movable or not). For a node moving at speed $\vec{w} = (w_1, w_2)$ and components for fluid velocity (u_1, u_2), this condition requires equality between both normal components for fluid and boundary. It can be written:

$$\left(\begin{Bmatrix} u_1 \\ u_2 \end{Bmatrix} - \begin{Bmatrix} w_1 \\ w_2 \end{Bmatrix}\right) \cdot \begin{Bmatrix} n_1 \\ n_2 \end{Bmatrix} = \vec{0}.$$

This condition will be imposed in a strong way, which means it will be directly included in the system of equations before resolution.

The way to do is to project velocity components in $(\vec{n}, \vec{\tau})$ space (normal and tangential vectors of wall boundary) through the transformation matrix Q

$$\begin{Bmatrix} u_n - w_n \\ u_\tau - w_\tau \end{Bmatrix} = [Q]\begin{Bmatrix} u_1 - w_1 \\ u_2 - w_2 \end{Bmatrix}. \tag{14}$$

In order to maintain conservation properties of the numerical scheme when a corner occurs in an interface, the normal and tangential vectors have to be modified consequently. As can be
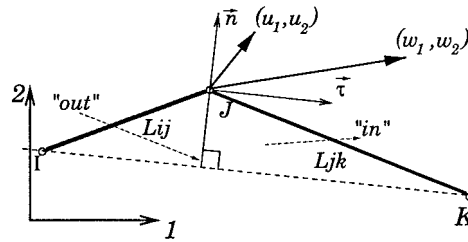
Figure 7. Choice of normal unit vector at a corner.

seen from Figure 7, the choice of projection of fluid velocity must be made in order to conserve spurious flux flowing in on portion L_{ij} and flowing out on portion L_{jk} as described in the figure.

Mathematical expression can be deduced from this energetic aspect but to reduce calculations we can simply note that the correct direction is given by the slope of the line joining the end points of segments L_{ij} and L_{jk} of the interface [10].

Concerning the interface conditions between both fluid and structure we have

$$x_{\text{fluid}}(t) = x_{\text{structure}}(t) \text{ on interface,}$$
$$\dot{x}_{\text{fluid}}(t) = \dot{x}_{\text{structure}}(t) \text{ on interface.}$$

(15)

The non-respect of any of these conditions can create a discontinuity between the velocity of the structure and that of the fluid mesh at the fluid–structure interface and disturb the energy exchange between the fluid and the structure.

3.4.3. Inflow and outflow boundaries. Concerning inflow and outflow boundary conditions, they are treated according to characteristic directions. It is based on the fact that flow information propagates along characteristic lines. The number of conditions to be prescribed on a boundary with normal $\check{n}$ depends on the sign of the eigenvalues (u_n, u_n, $u_n + c$ and $u_n - c$, with c the celerity and u_n the normal fluid velocity) of the Jacobian of $(F_1, F_2) \cdot \check{n}$. This number is equal to the number of positive eigenvalues for the inflow and to the number of negative values for the outflow. Consequently, for a 2D flow with cases of supersonic and subsonic flows, it leads to

– subsonic inflow: three conditions as pressure, temperature and flow direction
– supersonic inflow: four conditions as pressure, temperature and velocity components
– subsonic outflow: one condition, usually ambient external pressure
– supersonic outflow: zero conditions

Remark:
Pressure and temperature are usually determined with Hugoniot's relations using total pressure and temperature.

3.5. Fluid–structure model

The integrated fluid–structure model involving structure, fluid and mesh displacement may be summarized as follows:

(a) *Structure model* (cf. Section 3.1): Space discretization leads to the set of equations:

$$[M]\left\{\frac{\partial^2 u}{\partial t^2}\right\} + \{f_{\text{int}}(u, t)\} - \{f_{\text{ext}}\} = 0$$

and a Newmark temporal discretization associated with a Newton–Raphson algorithm gives

$$-\left[\frac{4}{\Delta t^2} \cdot M + K_T\right]\{\Delta u\} = \{R\},$$

where $\{u\}$ represents structure variables and $\{\Delta u\}$ the incremental solution between two time steps.

(b) *Mesh displacement* (cf. Section 3.2): One may construct a pseudo-material model for the mesh node motion by analogy with structure calculation. The unknowns $\{x\}$ correspond to mesh node co-ordinates and are calculated in imposing boundary displacements (previously computed in structural part) and solving a system such as

$$[\bar{M}]\left\{\frac{\partial^2 x}{\partial t^2}\right\} + [\bar{C}]\left\{\frac{\partial x}{\partial t}\right\} + [\bar{K}]\{x\} = 0,$$

with $\check{w} = (\check{x}^{p+1} - \check{x}^{p})/\Delta t$ the nodal mesh velocity; $[\bar{M}]$ the pseudo-mass matrix; $[\bar{C}]$ the pseudo-damping matrix; $[\bar{K}]$ the pseudo-rigidity matrix.

In this work, this aspect has not been considered but is only mentioned for a general case of fluid–structure interaction.

(c) *Fluid model* (cf. Section 3.4): Spatial discretization leads to

$$[M]^{p+1}\{U\}^{p+1} = [M]^p\{U\}^p + \{R\}^{p+1/2},$$

with $\{U\}$ the flow field variables.

We add a FCT technique that allows shock capturing in avoiding unwanted oscillations by the switch between high- and low-order solutions respectively in smooth and high gradient zones (cf. Section 3.3).

The solution strategy corresponds to solving a structural model for step '$p+1$' followed by mesh displacement calculation. For the same time step, we obtain the fluid flow field using mesh displacement, the boundary changes being obtained from structure solutions at step 'p' and $p+1$.

From a practical point of view, the coupling part concerns the establishment of a dialogue between the fluid and the structure codes. The use of *parallel virtual machines* (PVM) routines gives the possibility to alternatively run these codes keeping the modularity aspect of each one. These routines permit the exchange of values between different running codes in a simple way and with a minimum of modifications in the original programs. For the data exchanged see Figure 8.

The fluid and structure fields have often different time scales. In the case of the fluid–structure problem, the fluid flow requires a smaller temporal resolution than structure vibration. It
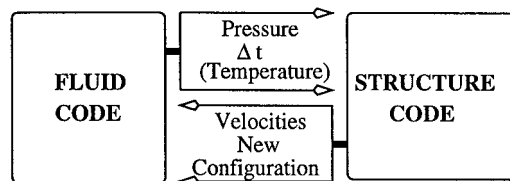

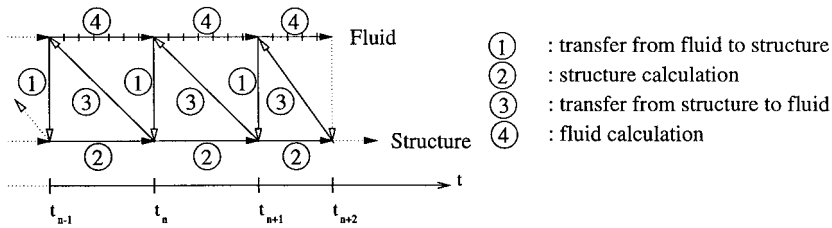Figure 8. Coupled codes and data transfers.

Figure 9. Coupling algorithm between structure and fluid codes.

is then advantageous to introduce subcycling into computing the new structure configuration after a given number of iterations for fluid $n_{f/s}$.

The choice of time steps for fluid and structure codes depends on the temporal schemes selected. In the present study, the temporal scheme for structure is implicit, whereas it is explicit for fluid. Presently, an active research is underway to develop a strategy for choice of coupling algorithm in order first to increase precision order and so to reduce numerical diffusion and secondly to find the best choice for $n_{f/s}$ [16,17].

The present strategy involves structural calculation followed by the fluid computation as shown in Figure 9.

4. NUMERICAL VALIDATION

In this section, a number of examples to validate this coupled model are presented. The numerical simulations include the following aspects:

1. validation of the Lax–Wendroff scheme with shock capture for a fixed mesh;
2. validation of geometrical consistency for a uniform flow;
3. validation of the ALE formulation;
4. validation of the coupled fluid–structure model.

4.1. Validation of the Lax–Wendroff scheme

4.1.1. Compression ramp in a supersonic flow. The objective of this example is to test the Lax–Wendroff scheme coupled with a FCT technique for shock capturing with an adaptive mesh technique.

The geometry is a compression ramp of 10° deviation angle. The free supersonic flow is given at a Mach number 3 with a static pressure equal to $1.0E + 05$ Pa and a temperature of 300 K. With these data it is thus possible to find a theoretical solution given in Figure 10.

The domain is 2.5×0.8 m^2, the ramp is located at 0.4 m if we consider the left boundary of the domain as the origin. The computation is initialized with the free flow condition as
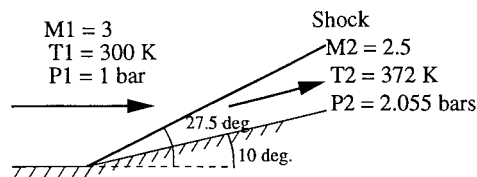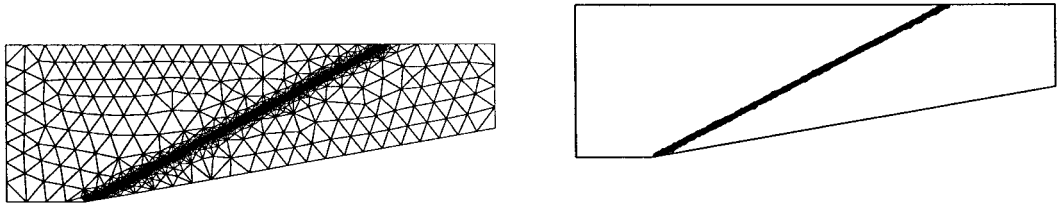

Figure 10. Compression ramp.

Figure 11. Adapted mesh and pressure iso-values.

mentioned, just above that which physically corresponds to suddenly imposing the ramp to the flow. The flow is maintained constant in time at the inflow boundary, a slip condition is imposed for the wall boundary. No condition is imposed at the outflow boundary since the flow is supersonic. The upper frontier is considered as a free-boundary.

An adaptive mesh technique is used in this example to locate precisely the compression shock in refining the mesh. This technique is based on the estimation of the local gradient and the estimation error calculations for each conservative variables [13,15]. The final mesh has been obtained after three successive remeshing steps and is composed of 1290 nodes and 2497 elements. It can be seen in Figure 11 that the adapted mesh on which the solution converged and the pressure field where the iso-values are all located near the shock.

The deviation angle corresponds exactly to the theory, the flow is uniform as upstream and downstream of the shock and corresponding pressure, Mach number and temperature match with the theoretical values.

The pressure and Mach number profiles at middle height are represented in Figure 12, the absence of oscillations around the shock displays the good shock capture by the FCT technique.

4.1.2. Rocket engine calculation. The flow in a rocket engine is directly controlled by the design of the section evolution. Two zones can be distinguished: the converging part allows the flow to accelerate until a Mach number equals 1 in the throat. The second part located after
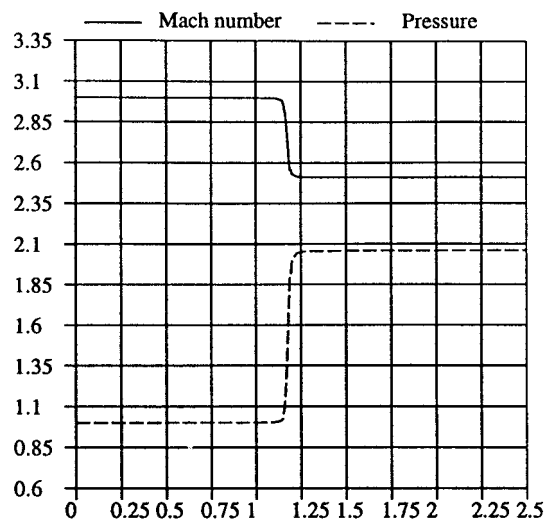

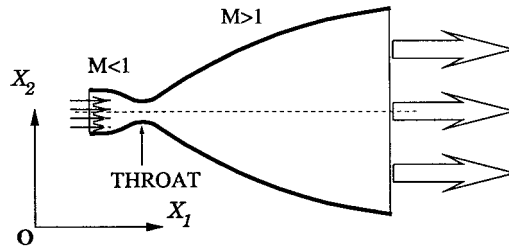Figure 12. Mach and pressure profiles at middle height.

Figure 13. Rocket engine.

the throat and called divergent is used to accelerate the fluid in the supersonic regime. The thrust of the rocket is directly proportional to the momentum of the outflow.

The test configuration given in Figure 13 is inspired from a rocket engine [18] but physical data and dimensions are purely academic. The dimensions are

– length = 1 m.
– inflow diameter = 0.4 m.
– throat diameter = 0.28 m
– outflow diameter = 1.1 m.

The total pressure is $P_T = 11$ MPa and the total temperature is $T_T = 2400$ K. This corresponds to the reservoir values.

Because of the flow symmetry, the calculation is made only on the lower half of the rocket to reduce calculation costs. The flow field is initialized with total pressure and temperature at the inflow boundary and the domain is imposed with Mach number = 0 and $p_\infty = 10^5$ Pa.

During the calculation, the inflow and outflow are treated with characteristic theory, a slip condition is imposed on the lower solid wall and the upper boundary is treated as a symmetry axis. The time step is computed with a CFL condition and corrected after each time step. A total of 2000 iterations is necessary to converge to steady state with a CFL number equal to 0.9.

Figure 14 presents the pressure profile on the axis and pressure iso-values field.

Figure 15 corresponds to the Mach number where the acceleration of the fluid is particularly visible on the Mach profile. The slope change in the nozzle wall in the throat region induces a barrel-like discontinuity that propagates in the supersonic region.
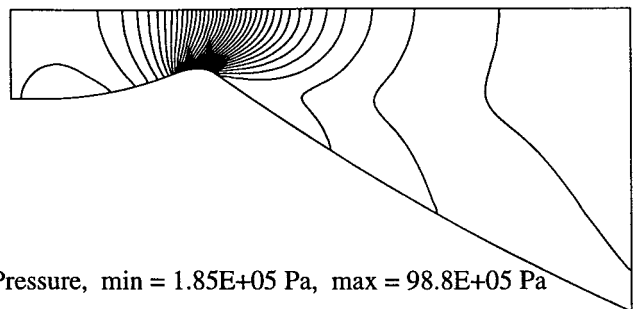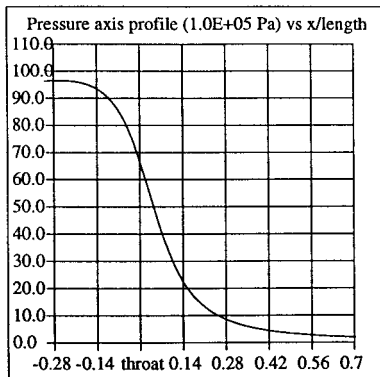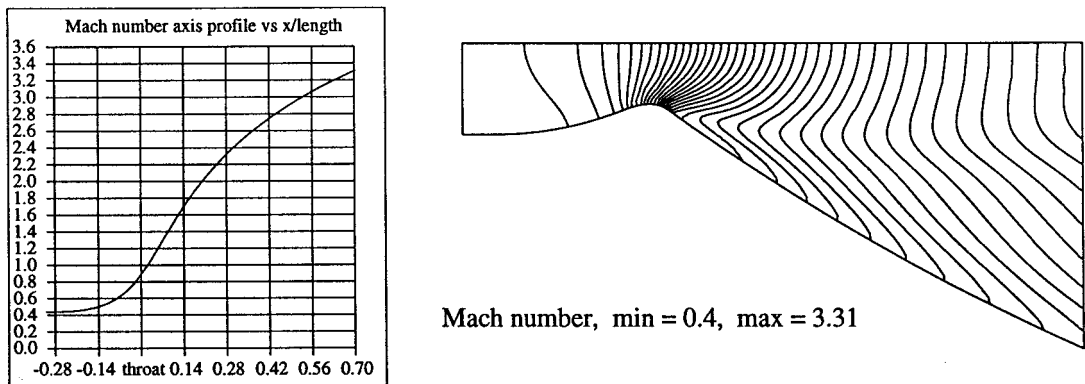

Figure 14. Pressure results.

Figure 15. Mach number results.

4.2. Validation of geometrical consistency for a uniform flow

The objective is to verify the consistency (*geometric conservation law*). The idea behind this numerical validation is to consider a uniform flow on a mesh described by an arbitrary geometry and to impose a temporal displacement of interior nodes keeping the boundary nodes fixed in time. During the calculation, the flow field and particularly the absence of extra velocity, which could be introduced by the mesh displacement in a case of violation of consistency or a bad implantation in the solver, are verified.

No graphical results will be given in this section, the previous solver being successfully tested in different numerical cases as, for example, with a square geometry and a radial and harmonic displacement of the interior nodes towards the centre of the domain in a uniform flow. The numerical solution reproduces exactly to uniform flow.

4.3. Validation of the ALE formulation

Two examples have been selected to test the ALE implantation in the code with a structure displacement known *a priori*. The first one concerns an adiabatic compression–expansion process [19]. This case offers the possibility to compare mass and energy conservation and physical behaviour with an analytical solution.

The second case concerns supersonic flow with a moving compression ramp where exact solutions can be found in the shock table.

4.3.1. Adiabatic compression–expansion process. The objective is to verify the mass conservation and the absence of hysteresis in the case of a reversible cyclic problem.

A compression–expansion process of a perfect gas kept in confinement in a cylinder closed by a moving piston is studied. The process is assumed to be reversible (successive quasi-static evolutions) and adiabatic. It is thus possible to obtain a theoretical solution assuming perfect gas and adiabatical process. During the process, the well-known relation between the pressure P and the volume V of the gas is given by

$$P \cdot V^{\gamma} = \text{constant, with } \gamma = 1.4.$$

The domain is a cylinder closed by a moving piston, as shown in Figure 16. The piston motion is governed by

Figure 16. Adiabatic compression–expansion process.

$$x_{\text{piston}} = cL + R(1 - \cos(\Omega t)) + \frac{R^2}{4L}(1 - \cos(2\Omega t)), \quad \Omega = 100 \text{ Hz}.$$

The initial conditions are $P_0 = 2.0\text{E} + 05$ Pa, $T_0 = 300$ K and velocity equals 0. Imposing the temporal evolution law of the piston, it is possible from initial conditions to obtain pressure and temperature histories

$$P(t) = P_0\left(\frac{V_0}{V(t)}\right)^\gamma, \qquad T(t) = \frac{P_0 V_0^\gamma}{R}\frac{1}{V(t)^{\gamma-1}}, \quad \text{with} \quad R = 8.32 \text{ SI and } V(t) = h \cdot x(t).$$

The mesh is composed of 650 elements and the time increment is based on a CFL condition. Natural adiabatical condition is conserved and slip condition is imposed for velocity components on solid boundaries. Calculations have been done for 1.5 cycles. At the end of each time step, the total mass is calculated and compared with the initial one.

The remeshing process is made by linear interpolation of node displacement between the fixed wall on the left and the moving wall on the right.

Averaged temperature and pressure are computed and monitored on T–P graph as shown in Figure 17, in collapsing both variables in the same graph in order to better verify accuracy and hysteresis phenomena if it exists (right figure).

The computational results reproduce exact solutions and it is observed in Figure 17 (right) and the absence of the hysteresis phenomenon, an essential condition for a reversible cyclic problem, is noted. The mass evolution is less than 0.2% and traduces the good conservative aspect of the scheme in a case where the ratio minimum/maximum volumes is equal to 0.3.

Figure 17. Volume–time and pressure–time results.

4.3.2. Moving ramp in a supersonic free stream. The objective is to test the moving mesh algorithm of the ALE formulation in considering a moving ramp, displacing itself within a supersonic flow field.

The domain is 2×0.7 m^2. The ramp length is 0.1 m with 10° inclination. The initial conditions correspond to a Mach number $M_1 = 2.25$, a pressure $P_1 = 1.0E + 05$ Pa and a temperature $T_1 = 300$ K. The ramp moves in the opposite direction (to the left) with a speed equivalent to a Mach number equal to 0.75. Theoretical results extracted from the shock table for an equivalent Mach number of 3 gives a shock deviation of 27.25° and a pressure $P_2 = 2.10^5$ Pa downstream the shock.

The initial conditions correspond to the free stream, the boundary condition being the same as that in the previous fixed case (first validation test). The remeshing process only consists of a vertical displacement of mesh nodes during passing ramp. The mesh is composed of 2603 nodes and 5104 elements. A CFL condition is used to assure stability and gives a time step size of $\Delta t \approx 1.0E - 05$ s for CFL = 0.9.

Results presented in Figure 18 for different positions of ramp collapse with good accuracy of the exact solution as well for the deviation shock angle as for physical properties like pressure, Mach and temperature upstream and downstream of the moving shock.

The first figure corresponds to the establishment of the shock and the rarefaction fan due to the horizontal plane following the ramp. On the others, they are established and follow perfectly the moving ramp. It can be observed too that during the ramp displacement, the deviation angle is maintained as well as the rarefaction fan. No dissipative effects are observed for a mesh with no particular refining elements. This test example shows the robust character of the ALE model with moving boundaries.
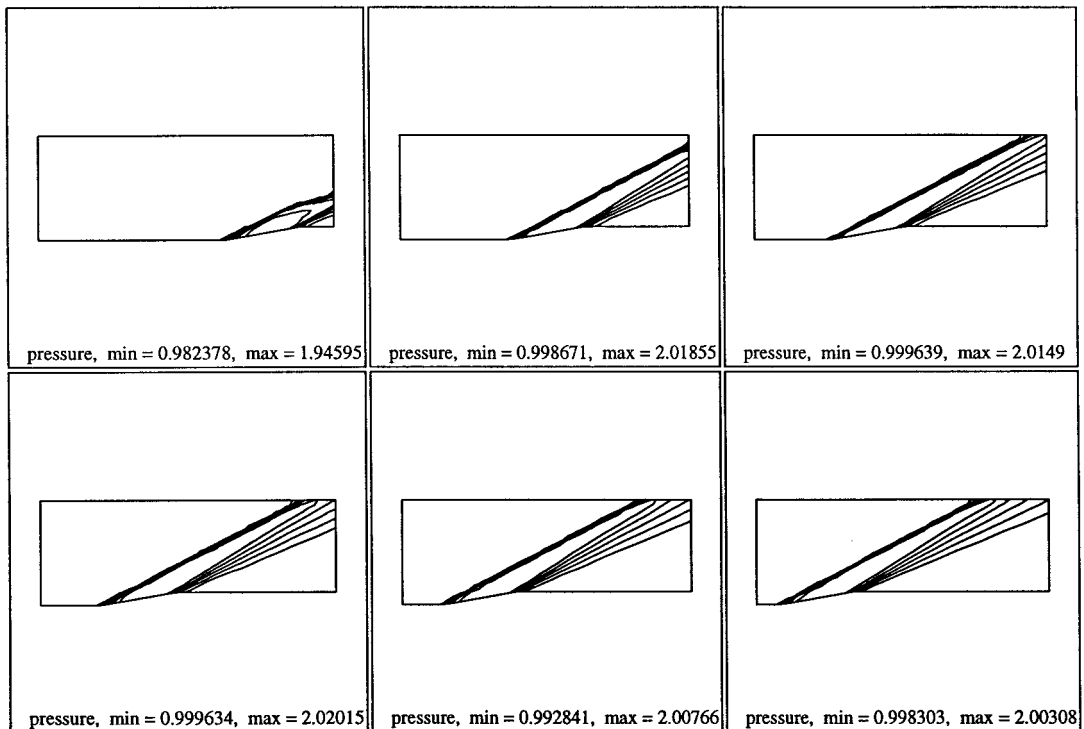

Figure 18. Moving compression ramp.

4.4. *Validation of the coupled fluid–structure model*

In this example, we couple the flow model with the structural deformation with ALE formulation. The objective is to investigate the energy transfer between structure and fluid at different instants. Indeed, the information exchanges between different physical domains are only based upon energetic transfers through internal, potential or different other kind of energy.

The principle 'nothing disappears or creates itself, anything is conserved or converted' means in a case of fluid structure interaction that what is lost by the fluid is transferred to the structure and *vice versa*. The idea is then to run a dynamic coupling case in computing external energies stored in each part to verify the energy conservation of the global system. The first thermodynamic principle specifies that total energy variation can only be due to external work and heat exchange. In an adiabatic case, only external pressure work has to be considered.

In order to understand the coupling phenomenon, two simulations are performed:

– linear structural behaviour.
– non-linear structural behaviour.

The material properties are chosen as follows:

Numerical case	Young's modulus N m^{-2}	Thickness m	Mass density kg m^{-3}
Linear case	1.0E11	0.04	9000
Non-linear case	5.0E10	0.01	5000

A typical rocket engine with geometrical characteristics is shown in Figure 19. In order to introduce reliable boundary conditions, only the interior part of structure undergoes elastic displacement (60% of the structure behind the throat) as shown in Figure 19. Displacement data will be extracted from three points of the flexible part of the rocket that are respectively located at 10, 30 and 50% of the total length behind the throat. They are respectively defined in Figure 19 by $p1$, $p2$ and $p3$.

The flow data are exactly the same as those given in the previous steady state case. The initial conditions are ambient temperature and pressure over the domain with zero flow. At the
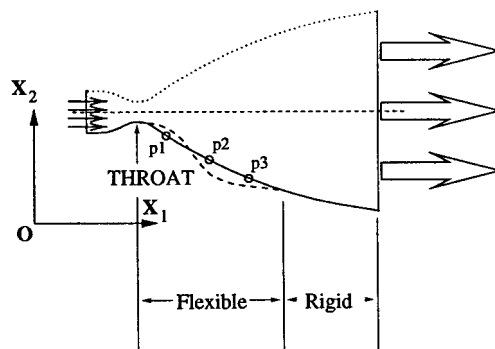
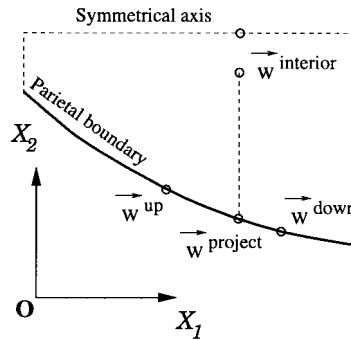

Figure 19. Rocket configuration.

Figure 20. remeshing technique.

inlet, boundary conditions are introduced that are compatible with total pressure and temperature. Slip conditions are imposed at the material boundary and the symmetrical axis. Inflow and outflow are calculated with characteristic theory. The fluid mesh is composed of 5721 nodes and 10952 triangular elements. The flexible part of the structure is composed of 131 nodes and 130 flat arch elements.

The mesh displacement of an interior node is obtained as follows (Figure 20):

1. For each interior node of the mesh, locate its vertical projection on the moving boundary and locate the parietal nodes up and down from this projection point.
2. From structure calculations, calculate the velocity of the projection $\vec{w}^{\text{project}}$. It involves interpolation between both up and down node velocities.
3. Calculate the $\vec{w}^{\text{interior}}$ by a linear interpolation between the projected node with $\vec{w}^{\text{project}}$ and associated symmetrical axis node with zero velocity.

4.4.1. Results for linear structural response. The free vibration analysis of structure gives the following four natural modes:

Natural mode	1	2	3	4
[Hz]	90	141	278	453

Figure 21 represents work performed by structure displacement (external energy) and fluid energy transfers during calculation. The x_1 displacements of points $p1$, $p2$ and $p3$ are also plotted (right part of the figure). In the same Figure, spectral description of energy and displacements evolutions are presented. An interesting aspect of this linear study is to verify that the first vibration mode of the structure contributes in a significant manner for energy transfer and structure displacement.

The authors make the following observations:

● First, the amount of external energy extracted by the structure is shown to be equal to that lost by the fluid, as it should be. In fact, the calculation after 20500 iterations leads to a difference between both energies of 2%. This can be reduced in sending to the structure code a pressure averaged over the $n_{\text{f/s}}$ fluid iterations rather than the last computed value.
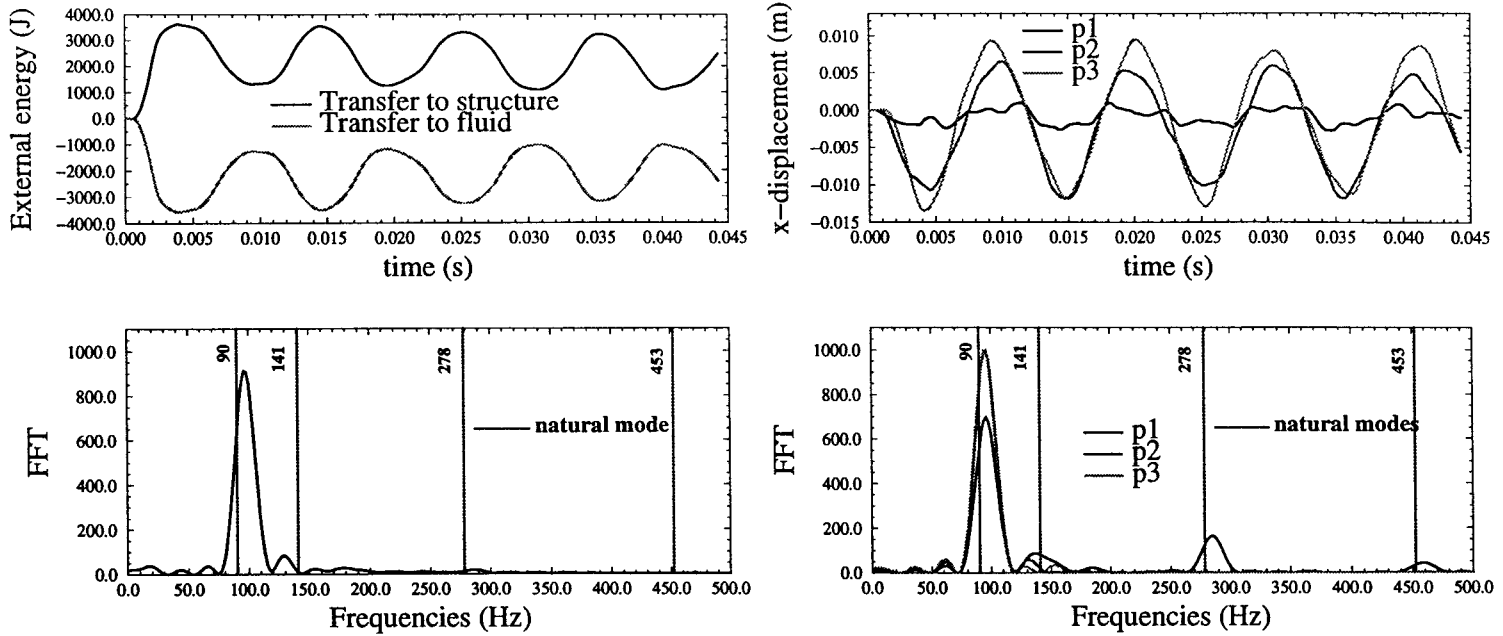
Figure 21. Energies and displacements histories for linear case.

- Secondly, a damping effect in the amplitude is due to numerical coupling scheme. Indeed, even if each code taken separately owns a second-order temporal accuracy, it is not the same for the coupling case. In order to avoid this, studies must be made for a correct coupling scheme in adding for example an intermediate data exchange between both codes, an idea that can be compared with a predictor–corrector scheme [9,17].
- The FFT representation gives a dominant frequency of 100 Hz, which is in effect near the fundamental frequency of the structure. It traduces the well-known fact that the first natural mode is the most energetic one and needs to be studied cautiously from a structure point of view when flutter behaviour is approaching in order to limit damages. For the figures concerning the displacement, the observations are the same except that the first four natural frequencies are excited by the fluid motion and can be observed on the graph. The result corresponds to experimental knowledge where the structure is excited with modal components near its natural frequencies when linear displacements are considered.

4.4.2. Results for non-linear structural behaviour. The next calculation is relative to the non-linear case. Consequently, no direct conclusion can be deduced. This example has to be considered as an academic test case. The iso-Mach values are given in Figure 22 for different instants ($\Delta t = 2.7\mathrm{E} - 03$ s): $t = 0.0027, 0.0054, \ldots, 0.02165$ s. A significant interaction with structure deformation may be observed as compared with the rigid structure case (see Figures 14 and 15). In Figure 23, the iso-values of the y-velocity for fluid flow for the same instants are given.

The motion and deformation of the parietal boundary inducing transformation in the flow field can be observed. It is particularly visible on the pressure jump that is sensitive in regard with wall motion. In a static case, this latter is due to the discontinuity of the derivative of degree 2 for the design after the throat.

The energy transfer and x_1 displacement evolution of the structure are given in Figure 24, always with their respective frequential representation. The linear natural modes of the structure are:

Natural mode	1	2	3	4	5
[Hz]	33.8	55.4	85.3	110	166

One can see clearly the non-linear coupling effects on the fluid flow behaviour due to large displacements of the structure. The following remarks can be made:

1. Natural modes are obtained after a linear analysis and with no external forces. In this case, external pressure is taken into consideration and displacements belong to the non-linear domain. The main visible effect when considering non-linear deformations is that it increases the rigidity of the structure. Indeed, the dominant frequency is around 65 Hz, whereas the first natural mode from linear analysis is around 34 Hz.
2. Henceforth, we have to consider the global system fluid + structure characterized by its own frequencies that can be different from the structure ones. It is then essential to predict the latter and to avoid global frequencies equal to any natural mode of the structure (especially the first one).
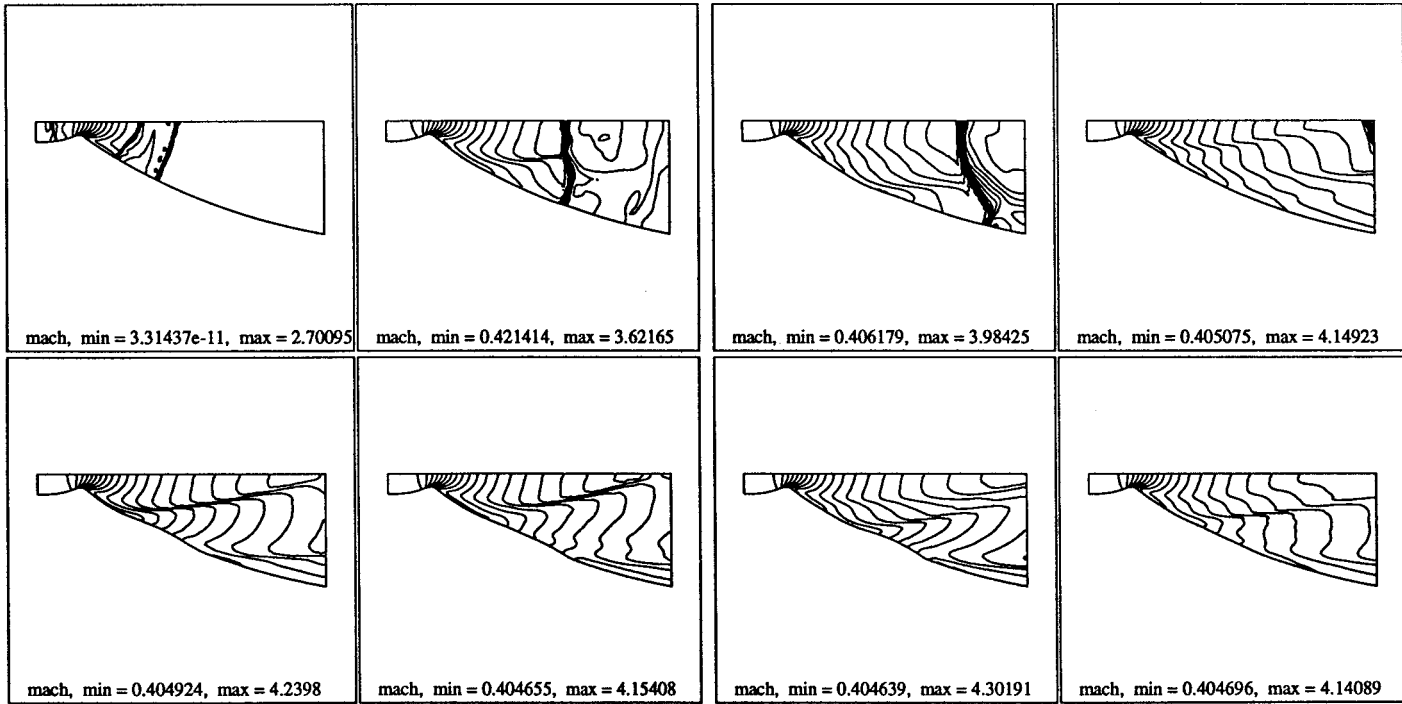
mach, min = 3.31437e-11, max = 2.70095

mach, min = 0.421414, max = 3.62165

mach, min = 0.406179, max = 3.98425

mach, min = 0.405075, max = 4.14923

mach, min = 0.404924, max = 4.2398

mach, min = 0.404655, max = 4.15408

mach, min = 0.404639, max = 4.30191

mach, min = 0.404696, max = 4.14089

Figure 22. Iso-values for Mach number in non-linear case.

v, min = -957.649, max = 240.134

v, min = -994.772, max = 227.209

v, min = -901.43, max = 224.759

v, min = -885.385, max = 224.725

v, min = -970.007, max = 224.633

v, min = -934.109, max = 224.741

v, min = -973.146, max = 224.799
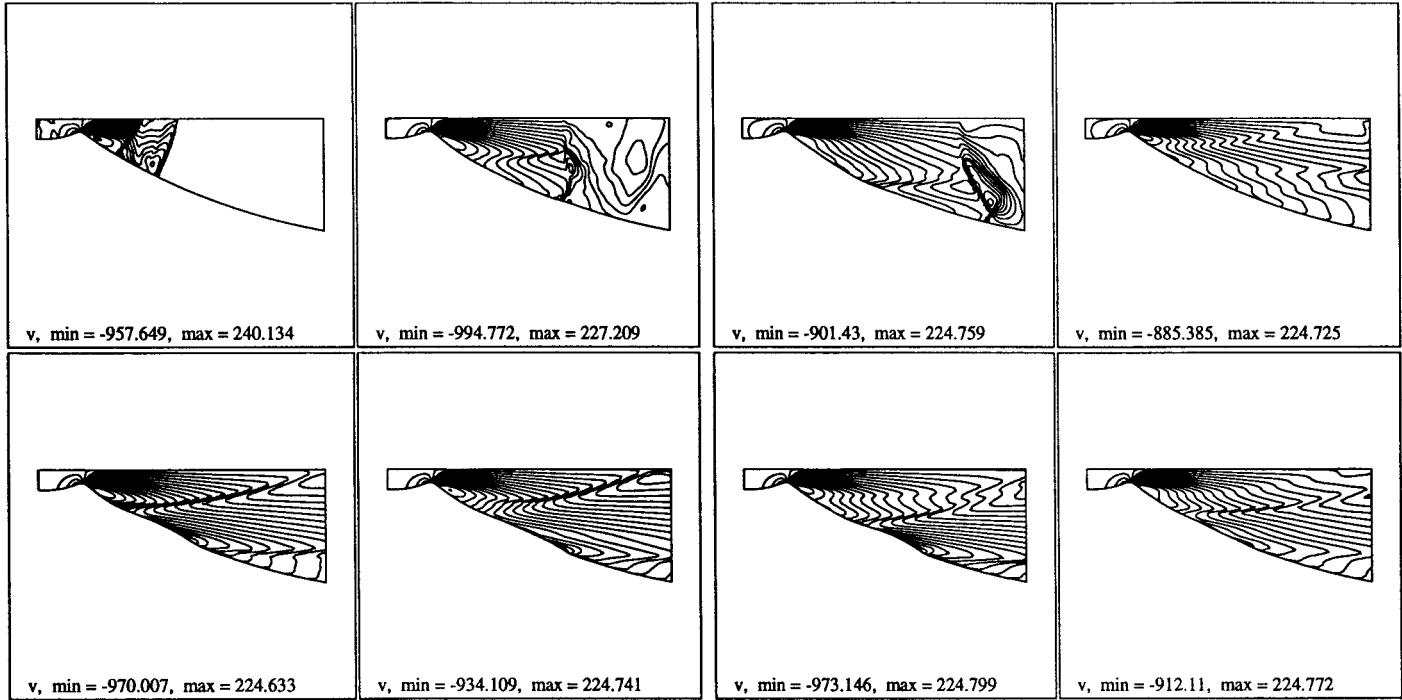
v, min = -912.11, max = 224.772
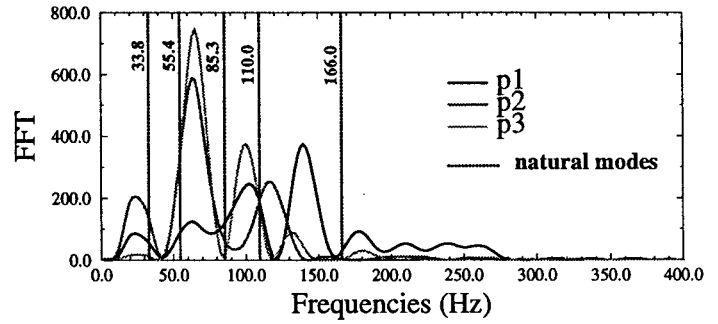
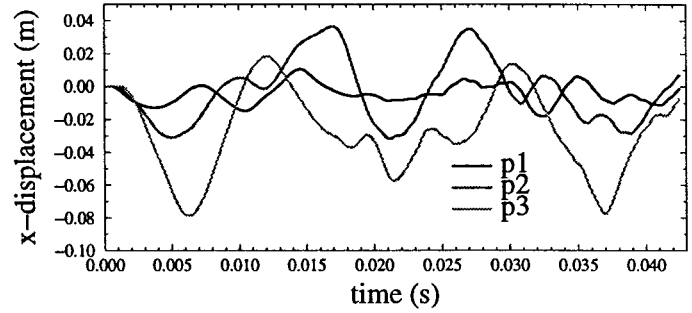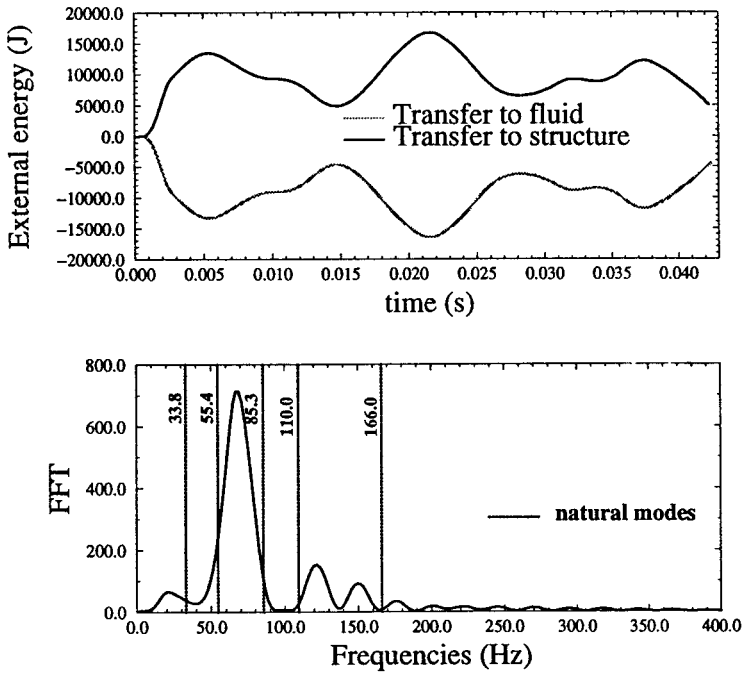Figure 23. Iso-values for y velocity in non-linear case.

Figure 24. Energies and displacements histories for non-linear case.

5. CONCLUSION

The main idea of this work was to develop a numerical model for fluid–structural interaction in combining existing numerical methods in a way they could rigorously keep their own qualities and easily be combined between one another. Some of the characteristics are:

– A compressible inviscid fluid behaviour is represented by an ALE finite element model using triangular elements.
– A beam arch element has been developed with large displacements and large rotations. The element includes shear effects as well.
– A second-order Lax–Wendroff scheme is employed to represent fluid space–time discretization. A FCT technique is introduced to capture shocks without oscillations. An automatic mesh refinement technique may also be implemented for high gradient zones.
– The mesh displacement respects the geometrical consistency. A uniform flow field is correctly reproduced for any moving mesh.
– A coupled fluid–structure model with large structural displacements has been implemented and tested for a number of academic cases. The model represents correctly the fluid–structure energy transfer with no unwanted dissipation.

At present, fluid–structure coupling is computed for the research of critical flow condition leading to a structure placed inside a flow to flutter in confrontation with linear theoretical results. The next objectives concern the introduction of viscous effects and the implantation of a turbulence model because of the fact that the main aspect in this kind of interaction is essentially energetical. A particular point will be the relation between the separation of the boundary layer and the side load effects occurring in rocket engines, which are able to cause material damages. As in reality with the phenomena being 3D, the extension in three dimensions of the previous solvers will be possible with regard to increasing capabilities of the actual computers.

REFERENCES

1. G. Dhatt and M. Fafard, 'Non-linear mechanic', *Tech. Rep.*, IPSI, September 1995.
2. G. Dhatt and M. Fafard, 'Resolution of non-linear problems', *Tech. Rep.*, IPSI, September 1995.
3. G. Dhatt and M. Fafard, 'Modelisation of shells in large rotations', *Tech. Rep.*, IPSI, September 1995.
4. T.J.R. Hugues and J. Winget, 'Finite rotation effects in numerical integration of rate constitutive equations arising in large deformation analysis', *Int. J. Numer. Methods Eng.*, **17**, 15–51 (1981).
5. S. Ammar, 'Résolution des problèmes non-linéaires', *Ph.D. Thesis*, Département Génie Mécanique, Université Laval, Québec, 1996.
6. J.L. Batoz and P. Lardeur *et al.*, 'Analyse non linéaire des structures minces par éléments finis', *Tech. Rep.*, U. T. Compiègne, Décembre 1985.
7. *ABAQUS—Theory Manual*, *Version 5.5*, K. Hibbit and R.I. Sorengen Inc., Pawtucket. 1992.
8. R. Löhner, 'An adaptive finite element solver for transient problems with moving bodies', *Comput. Struct.*, **30**, 303–317 (1988).
9. C. Farhat, 'High performance simulation of coupled non-linear transient aeroelastic problems', *Summer School-Porquerolles (France)*, July 1–6, 1996.
10. S. Giuliani, J. Donea and J.P. Halleux, 'An arbitrary Lagrangian–Eulerian finite element method for transient dynamic fluid–structure interactions', *Comput. Methods Appl. Mech. Eng.*, **33**, 689–723 (1982).
11. P.D. Thomas and C.K. Lombard, 'Geometric conservation law and its application to flow computations on moving grids', *AIAA J.*, **17**, 1030–1037 (1979).
12. G. Dhatt, A. Soulaimani, M. Fortin and Y. Ouellet, 'Finite element simulation of two- and three-dimensional free surface flows', *Comput. Methods Appl. Mech. Eng.*, **86**, 265–296 (1991).
13. M. Boulerhcha, 'Ecoulements Eulériens par eléments finis avec raffinement de maillage; comparaison d'un schéma centré et de schéma décentrés', *Ph.D. Thesis*, Département de Génie Mécanique, Faculté des Sciences et de Génie, Université Laval, Québec, 1993.

14. J. Peraire, R. Löhner, K. Morgan and M. Vahdati, 'Finite element flux-corrected transport for the Euler and Navier–Stokes equations', *Int. J. Numer. Methods Fluids*, **7**, 1093–1109 (1987).
15. S. Prudhomme, 'Adaptive finite element simulation of a supersonic underexpanded jet', *Master Report*, Faculty of the School of Engineering and Applied Science, University of Virginia, 1992.
16. B. Larrouturou, S. Piperno and M. Lesoinne, 'Analysis and compensation of numerical damping in a one-dimensional aeroelastic problem', *Tech. Rep.*, CERMICS, INRIA-Sophia-Antipolis, France, Juin 1993.
17. C. Farhat, S. Piperno and B. Larrouturou, 'Partitioned procedures for the transient solution of coupled aeroelastic problems. Part I: Model problem, theory and two-dimensional application', *Comput. Methods Appl. Mech. Eng.*, **124**, 79–112 (1995).
18. D. Vuillamy, A. Hadjadj and D. Vandromme, 'Simulation numérique des ecoulements dans une tuyère en présence de décollement', *Conf. Propulsive Flows in Space Transportation Systems*, Bordeaux, France, September 11–15, 1995.
19. Y.G. Lai and A.J. Przekwas, 'A finite volume method for fluid flow simulations with moving boundaries', *Comput. Fluid Dyn.*, **2**, 19–40 (1994).